Superior Stability of CsPbBr3 Films under High-Energy Proton Irradiation

Eduard Aleksanyan^{*,1}, Vachagan Harutyunyan¹, Anush Badalyan¹, Norayr Grigoryan¹, Narek Margaryan², Andranik Manukyan³, Lenrik Matevosyan⁴, Halyna Okrepka⁵, Vadim Trepalin⁵, Yang Ding⁵, Maksym Zhukovskyi⁶, Masaru Kuno^{5,7}, Ani Aprahamian^{5,7}, Khachatur Manukyan^{*7}

¹Applied Physics Research Division, ²Experimental Physics Division, and ³Isotopes Research and Production Division, A. Alikhanyan National Science Laboratory, 0036, Yerevan, Armenia
 ⁴Laboratory of Semiconductor Nanoelectronics, Institute of Radiophysics and Electronics, 0203 Ashtarak, Armenia
 ⁵Department of Chemistry and Biochemistry, ⁶Notre Dame Integrated Imaging Facility, and ⁷Department of Physics and Astronomy, University of Notre Dame, Notre Dame, IN, 46556 USA

Corresponding Authors

E-mail: aeduard@yerphi.am, Tel: +374 94 02 07 00 (E. Aleksanyan)

E-mail: kmanukya@nd.edu, Tel: +1 574 631 6083 (K. Manukyan)

ABSTRACT

This study examines the effects of high-energy (1.4 to 15.5 MeV) proton irradiation on CsPbBr₃ thin films, focusing on the significant transformations that occur beyond a critical dose threshold of 1×10¹⁵ protons cm⁻². Below this dose, the material maintains its structural and optical properties, demonstrating high irradiation stability. However, when exposed to doses exceeding this threshold, CsPbBr₃ undergoes notable changes, including the formation of CsPb₂Br₅, a decrease in bromine content, and significant particle growth, primarily driven by local thermal spikes and enhanced bromine mobility. The irradiation-induced particle growth improves photoluminescence characteristics and increases quantum yield and extended emission lifetimes due to reduced non-radiative recombination. These findings highlight the dual nature of CsPbBr₃ under proton irradiation: its inherent stability below a critical proton dose and its remarkable adaptive self-healing capabilities above it, underscoring its suitability for high-radiation applications.

1. INTRODUCTION

The power conversion efficiency of hybrid lead halide perovskite-based solar cells has significantly increased from 3.8% to 26%. These perovskites are not only easy to fabricate but also hold the potential to replace silicon in photovoltaic applications. However, the relatively low chemical stability of hybrid lead halide perovskites, such as methylammonium lead iodide (MAPbI₃) and formamidinium lead iodide (FAPbI₃), presents a significant hurdle to their utilization in solar cell technologies. 4,5

In contrast, inorganic lead halide perovskites such as CsPbI₃, CsPbBr₃, and CsPbCl₃ demonstrate enhanced chemical stability over their hybrid counterparts. The band gap of these perovskites can be precisely adjusted from 1.73 to 3.1 eV by formulating mixed anion perovskites with various I/Br or Br/Cl mixing ratios.^{6,7} This capability provides enhanced flexibility in optimizing the performance of solar cells. Moreover, CsPbBr₃ is favored as a top layer in both perovskite/perovskite and perovskite/silicon tandem solar cell designs due to its wider band gap (2.36 eV) than CsPbI₃ (1.73 eV).⁸

Lead halide perovskites are also emerging as promising materials for space-based solar cell applications due to their lightweight and mechanical flexibility. 9,10,11,12 These attributes could significantly reduce launch costs and offer versatility across various spacecraft designs. However, deploying these materials in space introduces challenges, particularly their sensitivity to environmental conditions such as temperature fluctuations and variations in vacuum, which could lead to material degradation. Furthermore, the impact of long-term radiation exposure, including from electrons and protons, on the structural changes of these materials remains an area that requires further investigation. 9,10,14,15

Radiation effects on hybrid lead halide perovskite solar cells have been studied extensively. ¹⁰ For instance, MAPbICl₂-based solar cells exhibit enhanced radiation tolerance compared to traditional silicon or III-V compound cells when subjected to a 1 MeV electron beam with a total dose of 1×10¹⁶ electrons cm⁻². ¹⁶ Notably, the charge carrier characteristics of MAPbI₃-based solar cells improve under irradiation of a 68 MeV proton beam at a dose of 1×10¹³ protons cm⁻² and flux of 1.7×10⁹ protons cm⁻² s⁻¹. This is attributed to the creation of shallow defect traps that mitigate deeper traps. ¹⁷ FAMAPb(I/Br)₃-based cells have also shown resilience against accumulated dose levels of 1×10¹⁶ and 1×10¹⁵ particles cm⁻² for electrons (1 MeV) and protons (50 keV), respectively. ¹⁸ Mixed-cation perovskite-based solar cells maintain their efficiency after exposure to proton irradiation doses up to 1×10¹³ protons cm⁻² at 150 keV. ¹⁹ Despite sufficient evidence demonstrating the resilience of perovskite solar cells against particle irradiation, the origins of this durability and occasional performance enhancements are not understood.

Several studies have attempted to investigate the radiation stability of bare perovskite materials to address these questions. For example, electron beam irradiation of MAPbI₃, FAPbI₃, and CsPbI₃ thin films has shown a correlation between the hardness of materials under electron beam irradiation and existing defects in pristine materials.²⁰ The exposure of CsPbBr₃ nanocrystals to a 200 keV electron beam in transmission electron microscopy (TEM) resulted in the desorption of Br and the reduction of Pb²⁺ to Pb.²¹ A quadruple cation perovskite subjected to 50 keV protons at doses above 1×10¹⁵ protons cm⁻² showed some degradation in photoluminescence (PL) without significant structural changes detectable by X-ray diffraction (XRD).⁹ These limited studies offer inadequate insights into the relationships between irradiation-induced structural changes and the optical properties of irradiated perovskites.

This work investigates the impact of proton irradiation on CsPbBr₃ thin films, with a focus on revealing the relationships between irradiation-induced structural modifications and optical properties, since protons are a primary source of damage in space.⁹ The films (thickness of 500 nm and an average grain size of 120 nm) deposited on a glass substrate were irradiated with varying proton energies ranging from 1.4 to 15.5 MeV, with a maximum dose of 5×10¹⁵ protons cm⁻² and an average flux of 1×10¹³ protons cm⁻² s⁻¹. The protons in these irradiation conditions have a minimum range of 26 µm in the glass substrate, ensuring a uniform distribution of atomic displacements within the films and avoiding the formation of dislocation loops or cavities (Supplementary **Figure S1**).

2. MATERIALS AND METHODS

Sample preparation. Cesium bromide (CsBr, 99.9%, Alfa Aesar) and lead bromide (PbBr₂, 98+% purity, Alfa Aesar) were employed to prepare CsPbBr₃ thin films using a double-source physical vapor deposition technique. The deposition process was conducted under a base pressure below 1.3×10⁻³ Pa. Precursors in equimolar amounts were placed in separate quartz crucibles and heated by distinct heat sources. Because both materials sublimate well, the evaporating temperatures were selected to be below the melting points of CsBr (635°C) and PbBr₂ (373°C). One-mm-thick glass substrates were pre-cleaned in an ultrasonic bath with acetone, deionized water, and semiconductor-grade isopropyl alcohol, then dried in flowing nitrogen. The substrates were placed on a rotating sample holder inside a vacuum chamber, positioned 10 cm from the evaporation sources. Deposition rates were set between 50 and 100 nm/min. After deposition, the films were annealed at 100°C for one hour. A large CsPbBr₃/glass sample was sectioned into multiple pieces for subsequent irradiation experiments, each measuring 1 × 1 cm. The samples

were stored in a dark, argon-filled desiccator to prevent possible light- and humidity-induced degradation during irradiation and characterization.

Proton Irradiation: The Cyclotron C18 (IBA, Belgium) at the Isotope Production Center of Armenia was used to irradiate samples with proton beams. No cooling systems were employed during irradiation. The proton beam energy was adjusted between 15.5 and 1.4 MeV by placing multiple molybdenum foils, each 50 μm thick, in front of samples. According to Stopping and Range of Ions in Matter (SRIM) simulations²² in this energy range, each foil reduces the proton energy by ~1 MeV. A Faraday cup is used to measure beam current and calculate proton flux before each sample irradiation. The irradiation dose at a given beam energy was achieved by varying the exposure times. The proton flux was maintained at an average of 1×10¹³ protons cm⁻² s⁻¹. Thin thermocouples were attached to the glass substrates to monitor temperature during irradiation. In some instances, activation occurred due to impurities in the glass substrate. Post-irradiation, the samples were observed using gamma-ray spectroscopy to assess any induced radioactivity.

Characterization. XRD analysis was conducted on a D8 Advance (Bruker) X-ray diffractometer operating at 40 kV and 40 mA with a Cu-K α radiation source. Measurements were taken in the Bragg-Brentano geometry, covering a 2 θ range of 10-50°. The step size was set to 0.02°, with a measuring time of 1 second per step. For a detailed view of the most intense peaks at higher resolution, a 2 θ = 28-32° range was recorded with a 0.01° step size and a 2 seconds per step measuring time.

Morphological investigations were conducted using a Magellan 400 field emission scanning electron microscope (SEM), which features secondary and backscattering electron detectors and a Bruker energy-dispersive X-ray spectrometer (EDS). Cross-sectional imaging and EDS

measurements were performed using a Talos F200i (Thermo Fisher Scientific) scanning TEM, operating at an accelerating voltage of 80 kV. The Talos was equipped with a Super-X EDS (Thermo Fisher) system containing a silicon drift detector with a spectral energy resolution below 136 eV for Mn–Kα (5.9 keV). Approximately 60 nm thin TEM samples were prepared using a Helios G4 UX (Thermo Fisher Scientific) dual-beam microscope with a gallium ion beam.

Optical measurements: Ultraviolet-visible (UV-Vis) absorption spectra of the samples were measured using an Agilent Cary 60 UV-Vis spectrophotometer in transmission mode. Measurements were conducted at room temperature in the 190-1100 nm spectral range. A continuous wave 405 nm laser (Obis, Coherent) was used to excite specimens for PL measurements. A typical irradiance was 3 W cm⁻². The resulting emission was collected and passed through a 425 nm long pass filter (Chroma). Spectra were acquired using a fiber-based spectrometer (Ocean Insight, USB2000).

PL quantum yield (PLQY) of films were estimated using a power-dependent PL approach described in the literature. In practice, this entailed exciting specimens at 460 nm with the output of an acousto-optical tunable filter-dispersed supercontinuum laser (NKT, 78 MHz, 13 ns). Specimens were mounted in an upside-down configuration in an inverted microscope (Nikon) to front-illuminate them. The resulting emission was subsequently filtered using a 473 nm long pass filter (Semrock) and was dispersed with a spectrometer (Acton), coupled to an electron multiplying charge-coupled detector (Andor). Spectra were acquired at different incident excitation intensities, ranging from 0.1-2500 W cm⁻² (peak irradiance) and were numerically integrated to yield an integrated emission intensity (I_{em}). Plots of I_{em}/I_{exc} versus I_{exc} were then fit to a kinetic model for QYs near peak values before the onset of Auger-induced non-radiative relaxation. The fit expression is $\frac{I_{em}}{I_{exc}} = \left[1 - \left(1 - QY_{opt}\right)\frac{1+I_{exc}}{2\sqrt{I_{exc}}}\right]$ and yields desired maximum QYs called QY_{opt}.

More about the power-dependent modeling of QYs can be found in References.^{23,24,25} Data acquisition was conducted using a purpose-written Python program.

The excitation source in time-resolved PL measurements was an acoustic-optical tunable filter-dispersed supercontinuum laser (Fianium, 40 MHz repetition rate, 4 ps pulse width). Samples were excited at 460 nm with typical irradiances of 2.5 nJ cm⁻² (peak irradiance). Collected emission was then filtered with a 485 nm longpass filter (Chroma) and detected using a single photon counting avalanche photodiode (MPD). A time-correlated single photon counting module (PicoQuant) was used to establish relative timings between excitation laser and detector pulses. Both instrument response function and lifetime data were acquired using low count rates to minimize pile-up effects.

Above measured decays were fit to single exponential or biexponential decays to extract average lifetimes (τ_{avg}). Radiative and non-radiative rate estimates were then made assuming first order kinetics. Specifically, τ_{avg} was expressed as $\frac{1}{\tau_{avg}} = k_r + k_{nr}$ with k_r and k_{nr} radiative and non-radiative rate constants. Obtained QYs were likewise expressed in terms of k_r and k_{nr} via QY = $\frac{k_r}{k_{nr}}$. From these expressions, effective k_r and k_{nr} were found through $k_r = \frac{QY}{\tau_{avg}}$ and $k_{nr} = \frac{1-QY}{\tau_{avg}}$.

3. RESULTS AND DISCUSSION

The XRD analysis of pristine films reveals that orthorhombic CsPbBr₃ is the dominant phase (**Figure 1A**). CsPbBr₃ displays a notable texture, predominantly aligning with the (002) crystallographic orientation. The average crystalline domain size, determined by the full width at half maximum (FWHM) of the diffraction peaks for CsPbBr₃, is 24±2 nm. The pristine films also contain a secondary tetragonal phase of CsPb₂Br₅. Rietveld refinement of the diffraction patterns

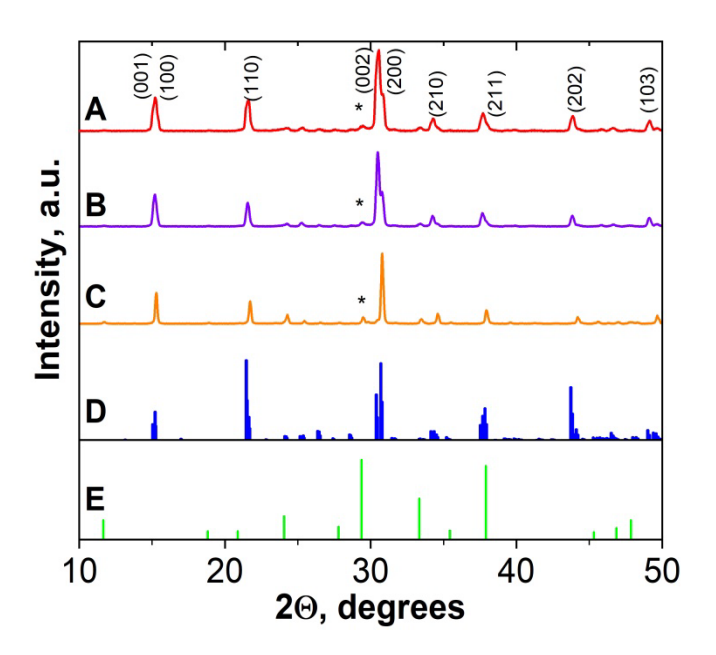


Figure 1. XRD patterns of pristine (A) and irradiated (beam energy of 15.5 MeV) CsPbBr₃ films with doses of 5×10^{14} protons cm⁻² (B) and 5×10^{15} protons cm⁻² (C). A diffraction peak ($2\Theta = 29.62^{\circ}$) for CsPb₂Br₅ is marked with (*). Calculated diffraction patterns for orthorhombic CsPbBr₃ (PDF#18-0364) and tetragonal CsPb₂Br₅ (PDF#25-0211) phases are also shown in panels (D) and (E), respectively.

Figure S2 and Table S1). Note that CsPb₂Br₅ often appears in vapor-grown thin CsPbBr₃ films.^{26,27}

Upon irradiation with a proton beam of 15.5 MeV and a dose of 5×10^{14} protons cm⁻², the films continue to show a texture with a preferred (002) orientation (**Figures 1B** and **S3**). However, the average size of the crystalline domains in the CsPbBr₃ phase increases to 28 ± 2 nm (**Figure S2** and **Table S1**). The CsPb₂Br₅ content in these irradiated films also rises slightly (6.5%). When exposed to a higher dose of 5×10^{15} protons cm⁻², the films lose their distinct texture, exhibiting random crystallographic orientations with a redistribution of intensities for (002) and (200) peaks (**Figures 1C** and **S3**), similar to polycrystalline powders.²⁸ The mean crystalline domain size for the CsPbBr₃ also increases to 38 ± 3 nm, and the CsPb₂Br₅ content reaches 10% (**Figure S2** and

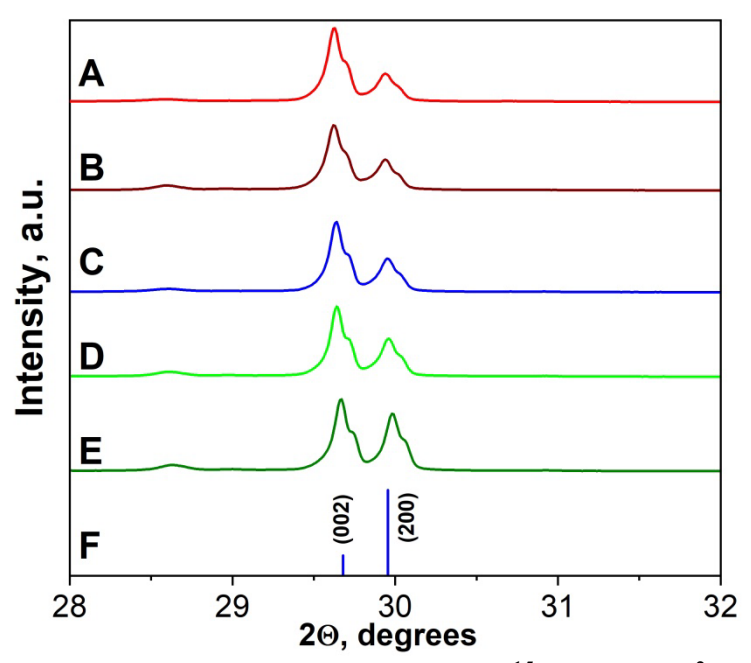


Figure 2. XRD patterns of pristine (A) and irradiated (1×10¹⁵ protons cm⁻² dose) CsPbBr₃ films with 12.5 MeV (B), 9 MeV (C), 6 MeV (D), and 1.4 MeV (E) beams energies. The calculated diffraction pattern (F) of orthorhombic CsPbBr₃ (PDF#18-0364) are also shown.

Table S1). The notable rise in CsPb₂Br₅ is likely linked to the water-activated radiolysis of CsPbBr₃.²¹ This connection is strengthened by the fact that the irradiation in our study was carried out under ambient conditions, with a relative humidity of 35%. These findings suggest a critical threshold dose of approximately 1×10¹⁵ protons cm⁻², beyond which irradiation alters considerably the structure of CsPbBr₃.

Variations in proton beam energy, while maintaining a constant dose near the critical threshold, have minimal impact on film structure. For example, lowering the beam energy from 12.5 to 1.4 MeV (at a dose of 1×10¹⁵ protons/cm⁻²) causes only a slight redistribution in the intensities of the (002) and (200) peaks (**Figure 2**). However, the average crystalline domain size in films irradiated at a beam energy of 1.4 MeV reaches approximately 39±3 nm (**Figure S2** and **Table S1**). This enlargement in domain size, with insignificant alterations in grain orientations, suggests beam-induced annealing. Simulations (**Figure S1**) support this hypothesis, indicating that

beams with reduced energy (e.g., 1.4 MeV) are stopped entirely within the glass substrate, unlike those at the highest beam energy (15.5 MeV). Such beam stopping in the glass could lead to beam-induced annealing at low-energy irradiation conditions.

A "plane-view" SEM image (**Figure 3A**) of a pristine film shows a densely packed particle morphology with a relatively narrow particle size distribution (**Figure S4**). The average particle size is approximately 120 nm. A cross-sectional bright-field TEM image reveals that primarily columnar particles have grown perpendicular to the substrate. Some of these particles extend up to 500 nm in length, reaching from the substrate to the film's surface. This TEM image also shows that some particles grow from adjacent ones. Unfortunately, the low stability of CsPbBr₃ under focused electron beams precluded electron diffraction measurements that would clarify the particles' orientations relative to their growth direction and orientation relationships among them. However, based on XRD analysis, we assume that the columnar grains are predominantly oriented

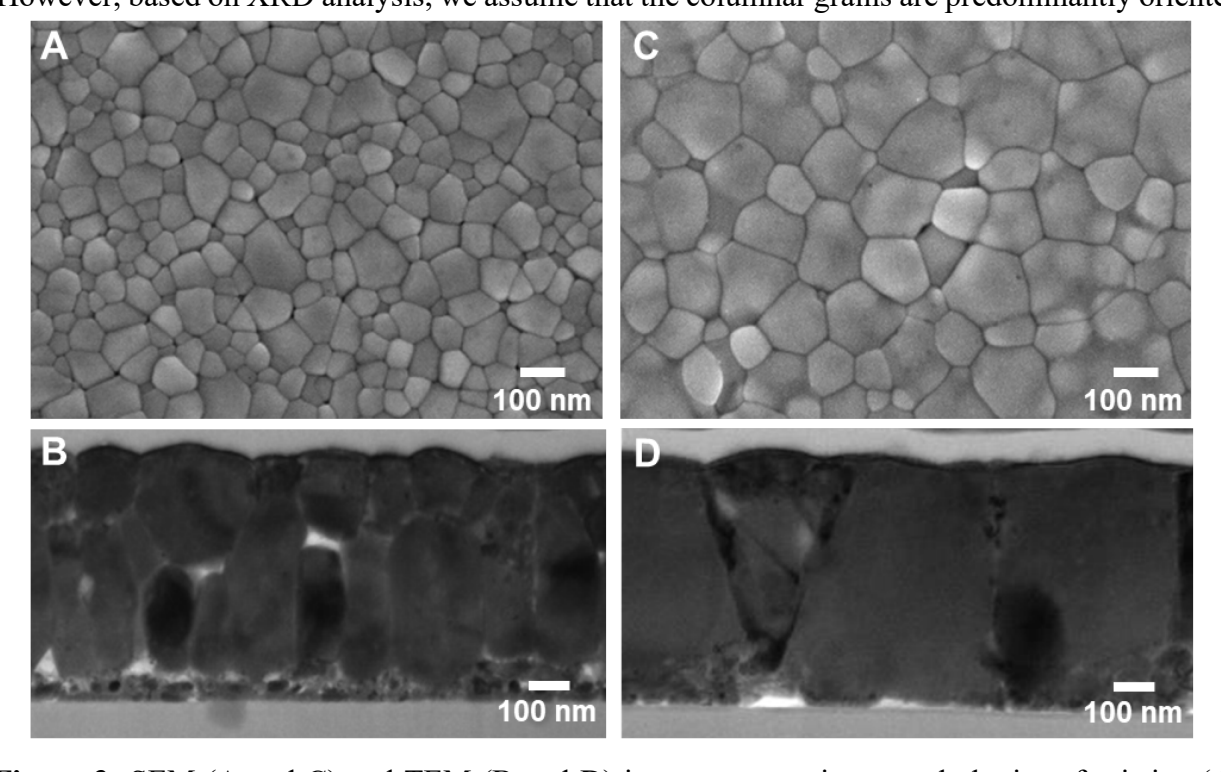


Figure 3: SEM (A and C) and TEM (B and D) images comparing morphologies of pristine (A and B) and a 15.5 MeV proton beam irradiated CsPbBr₃ with doses of 5×10^{15} protons cm⁻² (C and D) films.

along the (002) direction. We should also note that the Br/Cs ratio in pristine film measured by cross-sectional EDS is 3.06 ± 0.1 (**Figure S5**).

Detailed surface imaging revealed no noticeable voids or missing particles in irradiated films. This indicates the mechanical robustness of CsPbBr₃ under proton irradiation. These films maintain a closely packed structure, though the particles are considerably larger than in the pristine material. For instance, **Figure 3C** presents a representative SEM image of a film irradiated by a 15.5 MeV proton beam with a dose of 5×10¹⁵ protons cm⁻². This trend in particle growth is evident when comparing particle size distribution histograms (**Figure S4**). A film exposed to a dose of 5×10¹⁴ protons cm⁻² (at 15.5 MeV) has an average particle size of 250±100 nm, whereas at the highest dose of 5×10¹⁵ protons cm⁻², the particle size distribution widens, averaging 300±150 nm (**Figure S4**). Cross-sectional TEM imaging confirms significant particle growth, as shown in **Figure 3D**.

Particle growth may result from beam-induced heating. *In situ* measurements using microthermocouples (with a wire diameter of 100 μm) attached to the glass substrate indicated that the temperature remains below 60 °C during irradiation. We annealed the pristine films at temperatures up to 100 °C without beam exposure to evaluate the effects of pure thermal heating on particle growth. This annealing process did not alter the phase composition or film morphology. For instance, both annealed (**Figure S6**) and pristine films (**Figures 3A** and **S4**) display similar particle sizes, consistent with previously reported results.²⁹ These observations indicate that particle growth primarily occurs in an irradiation-induced regime independent of temperature.³⁰ This regime can be explained by the local thermal spike model, where the kinetic energy of recoil atoms (ions) is rapidly thermalized within localized regions.^{30,31} If a thermal spike occurs near a grain boundary, thermally activated atoms/ions within the spike region can transition across the

boundary. The local driving forces then cause a net movement of atoms in the direction that reduces grain-boundary curvature, resulting in boundary migration in the opposite direction.

Previously reported theoretical results suggest that V_{Br}^+ intrinsic vacancy defects in CsPbBr₃ have the lowest formation energy compared to V_{Cs}^- and V_{Pb}^{2-} .³² Moreover, the migration activation energies for Br $^-$ ions are significantly lower than those for Pb²⁺ and Cs^{+33,34,35,36}, suggesting that the high mobility of Br $^-$ ions could drive particle growth under proton irradiation within these spike regions. A slight decrease in bromine content, resulting from beam-induced volatilization in irradiated films beyond the critical dose threshold, indirectly supports this hypothesis. For instance, EDS analysis of such a film reveals a bromine-to-cesium ratio of 2.78 \pm 0.05 (**Figure S5**).

The morphological and structural changes in irradiated films indicate that we should be able to observe corresponding optical changes. UV-visible absorbance spectra (**Figure 4**) of pristine (spectrum A) and irradiated (spectra B and C) films display characteristic absorption features, including exciton absorption peaks at approximately 520 nm. These peaks are predominantly due to Wannier-type free cation excitons. 37,38 The exciton binding energy in CsPbBr3 thin films is ~ 40 meV 39 , which allows them to be detected at room temperature. It is noteworthy that some irradiated samples (e.g., at a dose of 5×10^{14} protons cm⁻²) exhibited an increased absorption background (**Figure S7**), attributed to irradiation-induced darkening of the glass substrate. This effect is corroborated by the similar high background observed in the absorbance spectrum of irradiated blank glass (**Figure S7**). The darkening results from the formation of color centers, which can be annealed during prolonged irradiation, such as at a higher dose of 5×10^{15} protons cm⁻², likely due to the associated heating. To ensure a direct comparison of absorbance spectra between irradiated and pristine films, we have subtracted the background from the irradiated blank

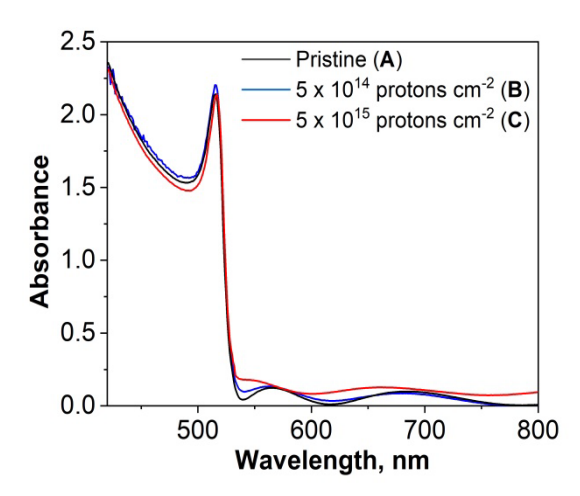


Figure 4. UV-visible absorbance spectra of pristine (A) and irradiated samples with a 15.5 MeV proton beam and doses of 5×10^{14} protons cm⁻² (B) and of 5×10^{15} protons cm⁻² (C).

glass substrates under the same irradiation conditions (**Figure S7**). UV-visible absorbance spectra of films irradiated with a lower proton beam energy and with a constant dose of 1×10^{15} protons cm⁻² exhibit features consistent with those observed in the changing dose series (**Figure S8**).

PL results under 405 nm laser excitation are presented in **Figure 5**. Bright PL of the pristine sample is observed with an emission maximum of 518 nm (**Figure 5A**). A narrow FWHM (~70 meV) confirms the relatively narrow particle size distribution. After irradiation with a dose of 5×10^{15} protons cm⁻² (15.5 MeV energy), the emission is redshifted by 5 nm (~ 23 meV). Here, a slight increase of FWHM (~78 meV) can be caused by larger particle size distribution compared to pristine samples. The reason for such a shift can be the appearance of defect levels created under irradiation slightly below the bottom of the conduction band.

Besides the redshift caused by irradiation, a significant enhancement of PL emission is also observed. PLQY increases from 39% for a pristine sample to 45% for an irradiated sample with 15.5 MeV and a dose of 5×10¹⁵ protons cm⁻². Such an increase suggests improvements to the

optical characteristics of irradiated films despite some structural degradation above the threshold dose.

The improvement in PL characteristics correlates well with a significant particle size increase and, therefore, a decrease in grain boundaries observed in our irradiated films. Grain boundaries between particles can act as recombination centers, shortening the average charge carrier diffusion length.^{40,41} Therefore, we expect that irradiated films with overall reduced grain boundaries will exhibit longer PL emission lifetimes than pristine films.

Lifetime measurements confirm this expectation. Irradiated films with an energy of 15.5 MeV and a dose of 5×10^{15} protons cm⁻² exhibit an average lifetime of up to ~1.7 ns compared to ~0.3 ns for pristine ones (**Figure 5B**). The decay curves of irradiated CsPbBr₃ films have been fit using biexponential functions with short ($\tau_1 = 0.65$ ns) and long ($\tau_2 = 2.5$ ns) components. Average lifetimes are reported. Extended average lifetimes over those of pristine films stem from order of magnitude changes to underlying radiative and non-radiative rates of irradiated specimens (Table

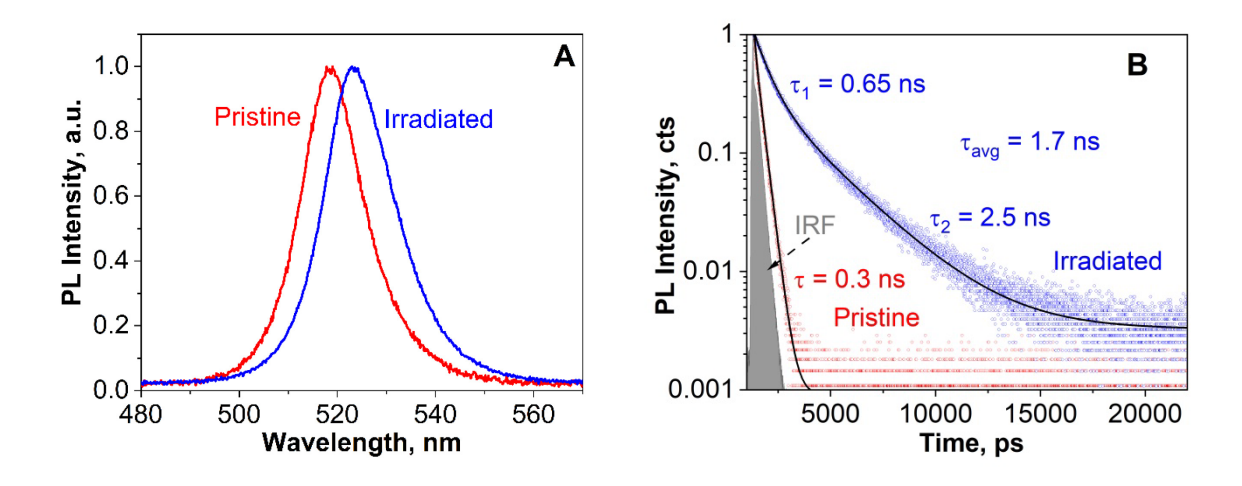


Figure 5. PL spectra (A) and PL lifetime measurements (B) results for pristine and proton irradiated films with energy of 15.5MeV and dose of 5×10^{15} protons cm⁻². The instrument response function (IRF) is provided in the B panel.

1). Similar decays, observed in hybrid lead halide perovskite films, have been attributed to surface and volume-related electron-hole recombination effects.⁴²

Table 1. Summary of optical responses of **CsPbBr**₃ thin films before and after proton irradiation, including effective first-order radiative and non-radiative rate constants.

	τ _{avg} (ns)	QY	$k_{\rm r}$ (s ⁻¹)	k _{nr} (s ⁻¹)
Pristine	0.3	0.39	1.3×10 ⁹	2.0×10 ⁹
Irradiated	1.7	0.45	2.7×10 ⁸	3.2×10 ⁸

The PL characteristics of irradiated films, even at doses exceeding the critical threshold of 1×10^{15} protons cm⁻², which exhibit increased levels of CsPb₂Br₅ and reduced bromine, underscore the unique "self-healing" properties of CsPbBr₃. Our findings align with prior studies demonstrating that self-healing of irradiation-induced damage occurs in CsPbBr₃ solar cells.⁴³ Previous research also indicates that CsPbBr₃ maintains robust performance under heat and light exposure, exhibiting minimal performance degradation even when solar cells face fluctuating environmental conditions.⁴⁴ This self-healing ability is attributed to the reversible decomposition and reconstruction of CsPbBr₃, facilitated by its high ionic mobility and relatively low formation energy.^{14,45}

4. CONCLUSIONS

In summary, this study reveals crucial correlations between proton irradiation conditions, structural changes, and optical enhancements in CsPbBr₃ thin films. When subjected to high-energy proton irradiation ranging from 1.4 to 15.5 MeV, especially beyond a critical threshold

dose of 1×10¹⁵ protons cm⁻², CsPbBr₃ undergoes significant structural and morphological transformations. These include partial water-activated radiolysis of CsPbBr₃ into CsPb₂Br₅, a reduction in bromine content, and notable particle growth. Particle growth is primarily driven by the high mobility of bromine ions under the influence of local thermal spikes induced by the high-energy protons. Enhanced PLQY and prolonged emission lifetimes in films irradiated above this critical dose are closely associated with reduced particle boundary areas, which diminish non-radiative recombination sites. The remarkable irradiation tolerance and self-healing capabilities of CsPbBr₃, attributed to its high ionic mobility, are vital for its stability under heat, light, and irradiation up to 1×10¹⁵ protons cm⁻². This resilience is critical to the long-term durability of solar cells in space, potentially supporting their operational viability for over 30 years.⁴⁶

ASSOCIATED CONTENT

Supporting Information (SI): The SI is available free of charge at:

SI contains SRIM simulations, additional XRD patterns, Rietveld refinement results, SEM images,
particle size distributions, EDS results, and UV-visible absorption spectra.

Note

The authors declare no competing financial interest.

ACKNOWLEDGEMENTS

The work was supported by the Science Committee of RA, in the frames of the research project № 21SCG-1C019 and 21T-1C232. The work also was partly supported by the Office of Naval Research Global (ONRG) grant No. N62909-22-1-2068. K.M. thanks U.S. Army Research

Office for Grant #W911NF2110045 under the Materials Synthesis & Processing Program, with Dr. Andrew Brown as the program manager. M.K. thanks the Division of Materials Sciences and Engineering, Office of Basic Energy Sciences, U.S. Department of Energy (DOE) under Award DE-SC0014334 and the U.S. National Science Foundation (DMR-1952841) for partial financial support of this work. The authors thank Artavazd Kirakosyan for the discussion.

REFERENCES

- 1. T, Miyasaka, A, Kojima, K, Teshima. Organometal halide perovskites as visible-light sensitizers for photovoltaic cells. *J. Am. Chem. Soc.* **131**, 6050–1 (2009).
- 2. Park, J. *et al.* Controlled growth of perovskite layers with volatile alkylammonium chlorides. *Nature* **616**, 724–730 (2023).
- 3. Tu, Y. *et al.* Perovskite Solar Cells for Space Applications: Progress and Challenges. *Adv. Mater.* **33**, 1–22 (2021).
- 4. Ava, T. T., Al Mamun, A., Marsillac, S. & Namkoong, G. A review: Thermal stability of methylammonium lead halide based perovskite solar cells. *Appl. Sci.* **9**, (2019).
- 5. Fan, Y. *et al.* Improving the stability of methylammonium lead iodide perovskite solar cells by cesium doping. *Thin Solid Films* **667**, 40–47 (2018).
- 6. Kovalenko, M. V., Protesescu, L. & Bodnarchuk, M. I. Properties and potential optoelectronic applications of lead halide perovskite nanocrystals. *Science* (80-.). **358**, 745–750 (2017).
- 7. Saran, R., Heuer-Jungemann, A., Kanaras, A. G. & Curry, R. J. Giant Bandgap Renormalization and Exciton–Phonon Scattering in Perovskite Nanocrystals. *Adv. Opt. Mater.* **5**, 1–9 (2017).
- 8. Kulbak, M., Cahen, D. & Hodes, G. How Important Is the Organic Part of Lead Halide

- Perovskite Photovoltaic Cells? Efficient CsPbBr₃ Cells. *J. Phys. Chem. Lett.* **6**, 2452–2456 (2015).
- 9. Kanaya, S. *et al.* Proton Irradiation Tolerance of High-Efficiency Perovskite Absorbers for Space Applications. *J. Phys. Chem. Lett.* **10**, 6990–6995 (2019).
- 10. Hoang, M. T., Yang, Y., Tuten, B. & Wang, H. Are Metal Halide Perovskite Solar Cells Ready for Space Applications? *J. Phys. Chem. Lett.* **13**, 2908–2920 (2022).
- 11. Pérez-del-Rey, D. *et al.* Perovskite Solar Cells: Stable under Space Conditions. *Sol. RRL* **4**, 1–6 (2020).
- 12. Olaleru, S. A., Kirui, J. K., Wamwangi, D., Roro, K. T. & Mwakikunga, B. Perovskite solar cells: The new epoch in photovoltaics. *Sol. Energy* **196**, 295–309 (2020).
- 13. Yang, J., Bao, Q., Shen, L. & Ding, L. Potential applications for perovskite solar cells in space. *Nano Energy* **76**, 105019 (2020).
- 14. Klein-Kedem, N., Cahen, D. & Hodes, G. Effects of Light and Electron Beam Irradiation on Halide Perovskites and Their Solar Cells. *Acc. Chem. Res.* **49**, 347–354 (2016).
- 15. Bose, S. *et al.* Unveiling Electron Dose-Induced Phase Decomposition and Energy Kinetics in Cu-Doped CsPbI₃ Nanocrystals. *ACS Appl. Nano Mater.* 7, 6020–6028 (2024).
- 16. Miyazawa, Y. *et al.* Evaluation of radiation tolerance of perovskite solar cell for use in space. 2015 IEEE 42nd Photovolt. Spec. Conf. PVSC 2015 4–7 (2015) doi:10.1109/PVSC.2015.7355859.
- 17. Brus, V. V. *et al.* Defect Dynamics in Proton Irradiated CH3NH3PbI3 Perovskite Solar Cells. *Adv. Electron. Mater.* **3**, (2017).
- 18. Miyazawa, Y. *et al.* Tolerance of Perovskite Solar Cell to High-Energy Particle Irradiations in Space Environment. *iScience* **2**, 148–155 (2018).

- 19. Barbé, J. *et al.* Radiation Hardness of Perovskite Solar Cells Based on Aluminum-Doped Zinc Oxide Electrode Under Proton Irradiation. *Sol. RRL* **3**, 1–8 (2019).
- Xiao, C. et al. Mechanisms of Electron-Beam-Induced Damage in Perovskite Thin Films
 Revealed by Cathodoluminescence Spectroscopy. J. Phys. Chem. C 119, 26904–26911
 (2015).
- Dang, Z. et al. In Situ Transmission Electron Microscopy Study of Electron Beam-Induced Transformations in Colloidal Cesium Lead Halide Perovskite Nanocrystals. ACS Nano 11, 2124–2132 (2017).
- Ziegler, J. F., Ziegler, M. D. & Biersack, J. P. SRIM The stopping and range of ions in matter (2010). Nucl. Instruments Methods Phys. Res. Sect. B Beam Interact. with Mater. Atoms 268, 1818–1823 (2010).
- 23. Draguta, S. *et al.* Spatially Non-uniform Trap State Densities in Solution-Processed Hybrid Perovskite Thin Films. *J. Phys. Chem. Lett.* **7**, 715–721 (2016).
- Wang, C., Li, C. Y., Hasselbeck, M. P., Imangholi, B. & Sheik-Bahae, M. Precision, all-optical measurement of external quantum efficiency in semiconductors. *J. Appl. Phys.* 109, (2011).
- 25. Zhang, Z. *et al.* Resonant Multiple-Phonon Absorption Causes Efficient Anti-Stokes Photoluminescence in CsPbBr₃ Nanocrystals. *ACS Nano* **18**, 6438–6444 (2024).
- 26. Caicedo-Dávila, S. *et al.* Effects of Postdeposition Annealing on the Luminescence of Mixed-Phase CsPb₂Br₅/CsPbBr₃Thin Films. *J. Phys. Chem. C* **124**, 19514–19521 (2020).
- Tong, G. et al. Phase transition induced recrystallization and low surface potential barrier leading to 10.91%-efficient CsPbBr₃ perovskite solar cells. Nano Energy 65, 104015 (2019).

- 28. Aleksanyan, E., Aprahamian, A., Mukasyan, A. S., Harutyunyan, V. & Manukyan, K. V. Mechanisms of mechanochemical synthesis of cesium lead halides: pathways toward stabilization of α-CsPbI₃. *J. Mater. Sci.* **55**, 8665–8678 (2020).
- 29. Palazon, F. *et al.* From CsPbBr₃ Nano-Inks to Sintered CsPbBr₃-CsPb₂Br₅ Films via Thermal Annealing: Implications on Optoelectronic Properties. *J. Phys. Chem. C* **121**, 11956–11961 (2017).
- 30. Kaoumi, D., Motta, A. T. & Birtcher, R. C. A thermal spike model of grain growth under irradiation. *J. Appl. Phys.* **104**, (2008).
- 31. Alexander, D. E. & Was, G. S. Thermal-spike treatment of ion-induced grain growth: Theory and experimental comparison. *Phys. Rev. B* **47**, 2983–2994 (1993).
- 32. Kang, J., Li, J. & Wei, S. H. Atomic-scale understanding on the physics and control of intrinsic point defects in lead halide perovskites. *Appl. Phys. Rev.* **8**, (2021).
- 33. Chen, C. *et al.* Ionic transport characteristics of large-size CsPbBr₃ single crystals. *Mater.*Res. Express 6, (2019).
- 34. Narayan, R. L. & Suryanarayana, S. V. Transport properties of the perovskite-type halides. *Mater. Lett.* **11**, 305–308 (1991).
- 35. Narayan, R. L., Sarma, M. V. S. & Suryanarayana, S. V. Ionic conductivity of CsPbCl₃ and CsPbBr₃. *J. Mater. Sci. Lett.* **6**, 93–94 (1987).
- 36. Mizusaki, J., Arai, K. & Fueki, K. Ionic conduction of the perovskite-type halides. *Solid State Ionics* **11**, 203–211 (1983).
- 37. Zazubovich, S. Physics of halide scintillators. *Radiat. Meas.* **33**, 699–704 (2001).
- 38. Protesescu, L. *et al.* Nanocrystals of Cesium Lead Halide Perovskites (CsPbX₃, X = Cl, Br, and I): Novel Optoelectronic Materials Showing Bright Emission with Wide Color Gamut.

- Nano Lett. 15, 3692–3696 (2015).
- 39. Wolf, C. & Lee, T. W. Exciton and lattice dynamics in low-temperature processable CsPbBr₃ thin-films. *Mater. Today Energy* **7**, 199–207 (2018).
- 40. Long, R., Liu, J. & Prezhdo, O. V. Unravelling the Effects of Grain Boundary and Chemical Doping on Electron-Hole Recombination in CH₃NH₃PbI₃ Perovskite by Time-Domain Atomistic Simulation. *J. Am. Chem. Soc.* **138**, 3884–3890 (2016).
- 41. Chu, Z. *et al.* Impact of grain boundaries on efficiency and stability of organic-inorganic trihalide perovskites. *Nat. Commun.* **8**, 1–8 (2017).
- 42. Zong, Y. W., Jian, B.-L. & Hsu, H.-C. Photoluminescence characterizations of highly ambient-air-stable CH₃NH₃PbI₃/PbI₂ heterostructure. *Opt. Mater. Express* **9**, 1882–1892 (2019).
- 43. Lang, F. *et al.* Radiation Hardness and Self-Healing of Perovskite Solar Cells. *Adv. Mater.*28, 8726–8731 (2016).
- 44. Akbulatov, A. F. *et al.* Light or Heat: What Is Killing Lead Halide Perovskites under Solar Cell Operation Conditions? *J. Phys. Chem. Lett.* **11**, 333–339 (2020).
- 45. Zhang, H. & Park, N.-G. Towards sustainability with self-healing and recyclable perovskite solar cells. *eScience* **2**, 567–572 (2022).
- 46. Markvart, T. Radiation damage in solar cells. J. Mater. Sci. Mater. Electron. 1, 1–12 (1990).

TOC Image

